Chemistry and Materials Research
ISSN 2224- 3224 (Print) ISSN 2225- 0956 (Online)
Vol 2, No.1, 2012

Influence of the $La_6W_2O_{15}$ Phase on the Properties and Integrity of $La_{6-x}WO_{12-\delta}$–Based Membranes

Mariya E. Ivanova[1*], Janka Seeger[1], Jose M. Serra[2], Cecilia Solis[2], Wilhelm A. Meulenberg[1], Werner Fischer[1,3], Stefan Roitsch[4], Hans Peter Buchkremer[1]

1. Forschungszentrum Jülich GmbH, Institute of Energy and Climate Research IEK–1 Leo–Brandt–Str., D–52425 Jülich, Germany

* E–mail of the corresponding author: m.ivanova@fz-juelich.de, m_encheva@abv.bg

2. Universidad Politécnica de Valencia – Consejo Superior de Investigaciones Científicas, Instituto de Tecnología Química, Av. Naranjos s/n, E–46022 Valencia, Spain

3. Forschungszentrum Jülich GmbH, Institute of Energy and Climate Research IEK–2 Leo–Brandt–Str., D–52425 Jülich, Germany

Ernst Ruska–Centre for Microscopy and Spectroscopy with Electrons, RWTH Aachen University and Forschungszentrum Jülich GmbH, Germany

The research is financed by the Initiative and Networking Fund of the Helmholtz Association (HA–104 MEM–BRAIN and Portfolio MEM–BRAIN), the German Federal Ministry of Education and Research (BMBF) for the Northern European Innovative Energy Research Project (03SF0330 N–INNER) and the Spanish Government (ENE2011–24761 grant).

Abstract

The aim of the present work is to evaluate the influence of $La_6W_2O_{15}$ secondary phase on the properties and integrity of $La_{6-x}WO_{12-\delta}$–based membranes. Structural, microstructural and thermo–chemical study was carried out evidencing significant crystallographic and thermal expansion anisotropy: the reason for poor thermo–mechanical stability of $La_6W_2O_{15}$. Conductivity of $La_6W_2O_{15}$ was one to two orders of magnitude lower compared to the phase pure $La_{6-x}WO_{12-\delta}$ in the range of 300 to 900 °C. The relaxation study showed that the hydration process was faster for the $La_6W_2O_{15}$ compared to the LWO phase, due to the higher electronic contribution to the total conductivity. Short–term stability tests in H_2 at 900 °C and in a mixture of CO_2 and CH_4 at 750 °C were conducted and material remained stable. Remarkable reactivity with NiO and YSZ at elevated temperatures was further evidenced compared to the relative inert behavior towards MgO and CGO.

Keywords: $La_6W_2O_{15}$, $La_{6-x}WO_{12-\delta}$, mixed protonic–electronic conductor, dense ceramic membrane, hydrogen separation.

1. Introduction

H_2/CO_2–gas separation by means of dense ceramic membranes is an advanced approach to realize the Carbon Capture and Storage (CCS) concept in the pre–combustion power plants (Jordal *et al.* 2004, Fontaine *et al.* 2007, Czyperek *et al.* 2010) along with the production of H_2 with high purity for a number of applications, e.g. electricity production, mobile applications, chemical industry, etc. ((a) Norby *et al.* 2006). High temperature proton conducting membranes could be integrated in, for example, catalytic membrane reactors, for non–oxidative coupling of methane and aromatization (Li *et al.* 2002) making possible the improvement of the process selectivity and efficiency by means of the in–situ removal of hydrogen.

In order to be efficiently implemented in H_2–separation tasks, materials have to exhibit mixed protonic–electronic conductivity and significant mechanical and thermal stability (Meulenberg, Ivanova *et al.* 2011, (a) Ivanova *et al.* 2012). Ceramic materials of several structural classes exhibit protonic and

electronic conductivity accompanied with considerable stability against CO_2–containing atmospheres. Amongst the material variety, acceptor–doped rare–earth oxides, e.g. Y_2O_3 (Norby *et al.* 1984, Norby *et al.* 1986), Ln_2O_3 (Balakrieva *et al.* 1989, Gorelov *et al.* 1990, (a) Norby *et al.* 1992, (b) Norby *et al.* 1992, Larring *et al.* 1995, Larring *et al.* 1997), rare–earth phosphates (Norby *et al.* 1995, Amezawa *et al.* 1998, Amezawa *et al.* 2004), pyrochlores (Shimura *et al.* 1996, Omata *et al.* 1997, Omata *et al.* 2004, Haugsrud *et al.* 2005, (a) Eurenius *et al.* 2010, (b) Eurenius *et al.* 2010), ortho–niobates ((a) Haugsrud *et al.* 2006, (b) Haugsrud *et al.* 2006, (b) Norby *et al.* 2006, Mokkelbost *et al.* 2008, Brandão *et al.* 2011, Huse *et al.* 2012, b Ivanova *et al.* 2012) and ortho–tantalates ((a) Haugsrud *et al.* 2007, Norby *et al.* 2007) can be mentioned. However, most of them do not show appreciable levels of electronic conductivity, or exhibit too restricted levels of protonic conductivity under the operating conditions relevant for the H_2–separation.

The state–of–the art oxides with perovskite structure (cerates and zirconates), especially their substituted forms, reveal the highest proton conductivity ($10^{-2} – 10^{-3}$ S.cm^{-1}), which upon an appropriate substitution can be further modified and reach appreciable levels of mixed conductivity and, respectively, H_2–flux at moderate to elevated temperatures (Meulenberg, Ivanova *et al.* 2011, (a) Ivanova *et al.* 2012). Cerates, however, suffer from insufficient stability in reducing and CO_2– and H_2O–containing atmospheres, whereas zirconates demonstrate better stability, but lower protonic conductivity due to the high grain boundary resistances (Meulenberg, Ivanova *et al.* 2010).

A novel class of ceramic materials: the rare–earth tungstates, having a general formulae $Ln_xWO_{3+1.5\cdot x}$ with x $\cong$ 6 (further referred as LnWO) and ordered defect fluorite (or disordered pyrochlore) structure (Chang *et al.* 1964, Mc Carthy *et al.* 1972), is recently at the research focus as a potential candidate for high temperature H_2–separation from gas mixtures.

Early study of Yoshimura *et al.* (Yoshimura *et al.* 1975) reported the electrical conductivities measured in the range of 500 to 1500 °C. It was shown that solid solutions in the system CeO_2–La_6WO_{12} exhibit predominantly electronic conductivity at high temperatures and ionic conductivity at low temperatures. No effects attributed to protons were considered and clarified in this study.

In 2001 Shimura *et al.* (Shimura *et al.* 2001) demonstrated that $La_xWO_{3+1.5\cdot x}$ (x $\cong$ 6, further referred as LWO) exhibits considerable proton conductivity under hydrogen–containing atmospheres. Proton conductivity of LWO–compound with stoichiometry $La_{5.8}WO_{11.7}$ was about $5\cdot10^{-3}$ S·cm^{-1} at 900 °C in wet H_2. The conductivity was also measured as a function of p_{O2} at 900 °C in wet atmospheres and a wide p_{O2}–independent region was observed meaning a broad ionic domain. At high p_{O2} a small increase of the conductivity was observed with a slope smaller than $(1/4)$ or $(1/6)$, suggesting limited p–type contribution. In the low p_{O2} regime, conductivity increases due to the n–type conductivity, resulting from W^{6+}–reduction.

Mixed protonic–electronic conductivity of both nominal and partially substituted LnWO with Ln = La, Nd, Gd, Er was furthermore evidenced by Haugsrud ((b) Haugsrud 2007). A comparison between the ambipolar conductivities of undoped LWO and 5%–Yb–substituted $SrCeO_3$, which is a state–of–the art mixed protonic–electronic material, came to the conclusion that the undoped LWO has a potential as a membrane material for separation applications (Haugsrud 2008).

The feasibility of the rare–earth tungstates as membrane materials for H_2 separation, in terms of the H_2 flow through them, was supported theoretically [33] based on the Wagner equation for H_2 flux (Eq. 1), where a membrane thickness of 10 μm and H_2 feed–side pressure of 10 atm were considered.

$$j_{H^+} = -\frac{RT}{2F^2}\cdot\frac{1}{L}\int_{\ln p'_{H2}}^{\ln p''_{H2}} \sigma_{H^+} t_e \, d\ln p_{H_2} \qquad (1)$$

Assuming that the H_2–transport through the membrane is dominated by the bulk diffusion mechanism, hydrogen permeation of about 2 $ml_n\cdot min^{-1}\cdot cm^{-2}$ was calculated for LWO at 800 °C. This value was higher than values similarly calculated for $SrCeO_3$ and Er_6WO_{12}: 1 $ml_n\cdot min^{-1}\cdot cm^{-2}$ and less than 0.1 $ml_n\cdot min^{-1}\cdot cm^{-2}$, respectively.

Several further works (Escolástico *et al.* 2009, (a) Escolástico *et al.* 2011, (b) Escolástico *et al.* 2011, Serra *et al.* 2012) determined experimentally the H_2 flux yielded by LnWO–based bulk membranes. The H_2 flux

across a $Nd_{5.5}WO_{12-\delta}$ membrane varies between $5\cdot10^{-3}$ and $5\cdot10^{-2}$ ml·min^{-1}·cm^{-2} measured at 1000 ºC (depending on the feed composition, i.e., H_2 vol.% and H_2O vol.%) ((b) Escolástico *et al.* 2011), while flux of up to 0.1 ml·min^{-1}·cm^{-2} was demonstrated for $La_{5.5}WO_{12-\delta}$ membrane. By doping of $La_{5.5}WO_{12-\delta}$ and $Nd_{5.5}WO_{12-\delta}$ using transition metals, it was possible to achieve flux value of above 0.3 ml·min^{-1}·cm^{-2} at 1000 ºC, which was the highest value reported for this class of materials.

In the chemical stability context, Shimura *et al.* (Shimura *et al.* 2001) commented that despite the transition nature of the W^{6+}–cations, $La_{5.8}WO_{11.7}$ is stable and no decomposition effects were detected after carrying out the electrochemical measurements in the range of 600 – 1000 °C.

According to ((b) Haugsrud *et al.* 2007), the chemical stability of rare–earth tungstates is their major disadvantage in terms of application. LnWO may react with carbon–containing gases and form stable carbides and oxycarbides. Nevertheless, Escolástico *et al.* (Escolástico *et al.* 2009) demonstrated good short term stability at 700 and 800 °C for Nd_6WO_{12}, which remained stable after exposure in both dry and humid gas flow consisting of 10 vol.% CO_2 and 90 vol.% CH_4 for 72 h.

Other issues might be related to the volatility of WO_x–species ((b) Haugsrud *et al.* 2007), which was considered as negligible in (Yoshimura *et al.* 1975), and to the high activity of La, possibly affecting the material stability against water vapor and CO_2. The evaporation of WO_x from LnWO becomes, however, an issue at higher temperatures and long–term operation regimes. As a consequence of the WO_x–volatility, LWO phase equilibrium shifts to the La_2O_3–rich region of the phase diagrams, according to phase studies on the binary system La_2O_3–WO_3 (Ivanova *et al.* 1970, Yoshimura *et al.* 1976). The unreacted and highly hygroscopic La_2O_3 readily forms $La(OH)_3$ with the atmospheric moisture, that practically leads to pulverization of a dense sintered sample in several hours. Figure 1 (a) documented this effect: a LWO–specimen sintered at 1450 °C for 24 h has pulverized after exposure to atmospheric air for several hours. Such negative deviations from the equilibrium can be effectively restricted and controlled during the material synthesis by W–overstoichiometry as reported in (Magrasó *et al.* 2009, Serra *et al.* 2012, Seeger, Ivanova *et al.*: article in preparation). Phase pure LWO was synthesized in the range of nominal La:W ratios $5.2 \leq x \leq 5.7$ (Magrasó *et al.* 2009). In spite of the minor experimental fluctuations falling out of this "single–phase" region, the most of the LWO–based materials prepared in our Labs (Seeger, Ivanova *et al.*: article in preparation) showed very good consistency with (Magrasó *et al.* 2009).

Another instability effect is observed, when the equilibrium is shifted to the WO_3–rich region of the phase diagram, resulting in formation of the secondary phase $La_6W_2O_{15}$, along with the main LWO phase. In order to prevent the possible sub–stoichiometry of La_2O_3, a proper pre–synthesis heat treatment of the La_2O_3 used as a raw material is particularly important. The formation of $La_6W_2O_{15}$ was reported in the early studies on the binary system La_2O_3–WO_3 (Ivanova *et al.* 1970, Yoshimura *et al.* 1976). Although these studies contain certain contradictions regarding to the LWO compound and its thermodynamic stability, which will not be discussed here, they all report the phase transitions of the $La_6W_2O_{15}$ phase with the temperature.

Based on the DTA measurements, two phase transitions were evidenced at 630 °C and 930 °C ($\alpha \xrightarrow{630^\circ C} \beta \xrightarrow{930^\circ C} \gamma$), according to Ivanova *et al.* (Ivanova *et al.* 1970).

Reversible thermal delays, detected at 619 °C and 929 °C on heating and at 598 °C and 922 °C on cooling, were reported by Yoshimura *et al.* (Yoshimura *et al.* 1976).

Similarly, Chambrier *et al.* (Chambrier *et al.* 2010) registered two endothermic peaks at 615 °C and 944 °C on heating and two exothermic peaks at 586 °C and 918 °C on cooling, respectively. The high temperature X–Ray Diffraction (HT–XRD) study showed furthermore shifts in the phase transition temperatures ($\gamma \xrightarrow{600^\circ C} \beta \xrightarrow{960^\circ C} \alpha$) compared to the early studies (Note 1).

Furthermore, the high temperature α–$La_6W_2O_{15}$ was an object of *ab–initio* computational study based on the *in–situ* HT–XRD and Neutron Powder Diffraction (NPD) data (Chambrier *et al.* 2010). A structural model of the α–polymorph was elaborated, according to which, the α–$La_6W_2O_{15}$ structure comprises both ordered and disordered groups and structural similarities were suggested for the two other polymorphs, β and γ, as well.

As observed in our Labs, the presence of the secondary phase $La_6W_2O_{15}$ in the LWO–bulk matrix was inevitably associated with an intensive crack formation that practically hinders the manufacturing of

gas–tight LWO–based membranes or other functional components. Figure 1 (b) shows a micrograph of a LWO bulk membrane, containing impurities of the secondary phase $La_6W_2O_{15}$. It can be clearly seen that the cracks are located in the areas identified as $La_6W_2O_{15}$, while the main LWO phase exhibits dense microstructure.

In the context of the discussed instability issues described in the literature and based on our practical experience with the LWO–based material, the present study on the functional characteristics of $La_6W_2O_{15}$ was strongly motivated to enlighten the overall influence of this secondary phase on the properties and integrity of the targeted LWO–based ceramics.

2. Experimental

2.1 Sample preparation

Powder of $La_6W_2O_{15}$ was synthesized of La_2O_3 (99.999%, Sigma–Aldrich, CAS 1312–81–8) and WO_3 (99.9%, Fluka) via the solid state reaction. Prior to weight, La_2O_3 was dried and decarbonated at 1000 °C for several hours. Stoichiometric amounts of the corresponding oxides were weighted, mixed and milled in ethanol. The resulting suspension was dried until complete ethanol evaporation. The synthesis took place in closed Pt crucibles at 1000 °C for 12 hours with heating and cooling ramps of 3 $K \cdot min^{-1}$. The product of the solid state reaction was then wet milled in ethanol, dried and grinded in agate mortar. Thus obtained powder was used for chemical composition verification and structural investigations, as well as for carrying out the stability tests and the chemical compatibility experiments.

Powder samples used for the chemical compatibility tests were prepared by mixing of previously synthesized single phase $La_6W_2O_{15}$ powder with the oxides CGO (CeO_2 doped with 20 mol.% Gd_2O_3, Treibacher, Austria), YSZ (ZrO_2 doped with 8 mol.% Y_2O_3, UCM Advanced Ceramics, Germany), NiO (99.0% min., J.T. Baker, USA) or MgO (99.995%, Sigma Aldrich) in weight ratio of 1:1. After mixing in a mortar the resulting powders were heat treated for 12 hours at temperatures ranging from 800 °C to 1400 °C. The products were finally grinded and phase composition was studied by means of the X–ray powder diffraction (XRD).

Pellets used for the microstructural studies, as well as for measuring the electrical conductivity *vs T* and p_{O2}, were prepared by the uni–axial pressing and sintered in air at 1400 °C for 12 hours with heating and cooling ramps of 2 $K \cdot min^{-1}$. Sintered specimens with 21 mm diameter and 1.3 mm thickness were coated with platinum paste (Ferro GmbH) for the electrical measurements and additionally heat treated at 1000 °C/2 h and 1200 °C/2 h. Bar–shaped samples with dimensions of 40x4x1 mm^3 were used for the conductivity relaxation study. As electrodes, 4 Ag–wires were contacted to the bar by means of Ag–ink and consequently heat treated.

2.2 Characterization techniques

Stoichiometry of the synthesized $La_6W_2O_{15}$ powder was controlled via the ICP–OES (Inductively Coupled Plasma – Optical Emission Spectrometry). No deviations from the nominal chemical composition could be detected.

Phase composition and thermal stability of the compound prepared by the solid state reaction were investigated by room temperature and in–situ high–temperature XRD.

Room temperature measurements were carried out using a Bruker–AXS D4 powder diffractometer in Bragg–Brentano scattering geometry with Cu–Kα radiation. Patterns were acquired between 10° and 80° 2Theta with a stepwidth of 0.02° and a diffracted beam monochromator. The software package X'Pert HighScorePlus 3.0 (Panalytical B.V., the Netherlands) was used for phase identification (ICDD PDF2 Release 2004). Lattice parameters were refined applying Pawley and LeBail method (Bruker–AXS TOPAS 4.2), assuming an orthorhombic unit cell.

A D5000 X–ray diffractometer (Siemens, Germany) equipped with a HDK S1 high–temperature chamber (Buehler, Germany) and a diffracted beam monochromator was used to study the phase stability in air as a function of the temperature. Scans were taken in the Bragg angle range from 18° to 49° (Cu–Kα radiation), in which the relevant reflections of the studied phase were located. In order to achieve a homogenous thin dense

layer for this study, the powder was deposited onto a *dc*–heated Pt strip via sedimentation from ethanol slurry. HT–XRD scans were recorded in the temperature range from 100 to 1100 °C in steps of 50 °C and heating speed of 3 $K \cdot min^{-1}$ between the temperature steps. 10 min delay time was applied before starting a scan at each temperature for achieving thermal and thermodynamic equilibrium. The same temperature program was realized in the cooling mode.

The microstructure of sintered samples was characterized by means of SEM and TEM. SEM was carried out using a FEI Helios Nanolab 400s and a Zeiss Ultra55 electron microscope. The TEM specimen preparation was performed by Focused–Ion Beam process (FIB, FEI Helios Nanolab 400s) with subsequent argon–ion milling. The TEM investigation was carried out by means of a FEI Tecnai G2 F20 instrument, operated with an acceleration voltage of 200 kV and equipped with an EDAX energy dispersive X–ray spectrometer.

The total *ac*–electrical conductivity of $La_6W_2O_{15}$ was measured at fixed frequency (11.9 kHz) as a function of temperature and oxygen partial pressure (p_{O2}). Temperature dependence was studied in the range of 300 to 900 °C for 6 different atmospheres: both wet and dry Ar, (4%H_2–Ar) and synthetic air. Saturation of 2.5 vol. % H_2O was achieved by bubbling the gas through water at room temperature. For drying the gas, commercial molecular sieve was used as a desiccant. The p_{O2} dependence of the conductivity was investigated at selected temperatures by mixing synthetic air and Ar under dry conditions by means of the ProGasMix™ (NorECs, Norway) (Norby 1988). The disc–shaped sample, initially contacted with Pt, was mounted in the ProboStat™ holder (NorECs, Norway) and 4 Pt–wires were connected pairwise to it. The conductivity was measured with the Alpha–A High Performance Frequency analyzer (Novocontrol Technologies GmbH, Germany) equipped with ZG4 test interface and controlled by the WinDeta software. Oscillation voltage of 0.4 Vrms was applied to the sample. The sample was heated to 900 °C with a ramp of 7.5 $K \cdot min^{-1}$ in the corresponding atmosphere and it was held at this temperature for 8 h. Then the frequency sweeps were recorded in the range of 100 Hz to 10 MHz downwards to 300 °C with T–steps of 25 °C and holding time of 0.5 h at each temperature. A stray capacitance of 5 pF, originating from the measurement rig, was subtracted from the raw data. For seek of reproducibility, the measurements were repeated three times under the described experimental set of conditions, each time using a fresh sample, and the obtained results matched very well.

Conductivity relaxation experiments were performed using a 4–probe bar configuration by means of PSM 1735 with an IAI interface from Newtons4th Ltd. A 100 Hz constant frequency was selected in order to avoid electrode contributions to the resistance. Measurements were performed from 450 to 750 °C in air by switching from dry to wet (2.5 vol. % H_2O) conditions in a very fast step of ~5 s: time negligible with respect to the conductivity relaxation time (Solís *et al.* 2011). Monitoring was carried out by means of a Balzers mass spectrometer.

The chemical compatibility of $La_6W_2O_{15}$ with CGO, YSZ, NiO and MgO was studied by XRD using D4 ENDEAVOR diffractometer by Bruker AXS with Cu–Kα radiation. Patterns were recorded between 10° and 80° 2Theta with a stepwidth of 0.02°. The software package X'Pert HighScorePlus 3.0 (Panalytical B.V./Netherlands) has been used for phase identification (ICDD PDF2 Release 2004).

The chemical stability of $La_6W_2O_{15}$ against carbonation and reduction was tested in two short–term experiments. During the first test, 1 g of $La_6W_2O_{15}$ powder was exposed to the action of wet (2.5 vol.% H_2O) gas mixture consisting of 10 vol.% CO_2 and 90 vol.% CH_4 for 72h at 750 °C. The second test was carried out with 1 g of $La_6W_2O_{15}$ powder exposed to wet H_2 (2.5 vol.% H_2O) for 55 h at 900 °C. The post–treatment XRD analysis of the powder material was carried out by a PANalytical X'Pert PRO diffractometer, using Cu–Kα radiation and a X'Celerator detector in Bragg–Brentano geometry in order to detect changes in the crystal structure of the material or formation of new phases as a result of the exposure to the experimental conditions.

3. Results and discussion

3.1. Structural characterization

3.1.1. Phase analysis

Figure 2 shows a typical Bragg–Brentano scan of the $La_6W_2O_{15}$ powder manufactured by the solid state reaction at 1000 °C/12 h. A single phase material was formed. The absence of an amorphous background and

the clear sharp reflections with a narrow full width at half maximum (FWHM) indicate a high degree of crystallinity and lattice perfection. All reflections could be indexed as belonging to the orthorhombic γ –$La_6W_2O_{15}$ (PDF 99–000–0026). This result is in a good agreement with data reported at 40 °C by Chambrier *et al.* (Chambrier *et al.* 2010).

3.1.2. Structural transformations and microscopic thermal expansion coefficients

Figure 3 (a) is a pseudo–3D plot of the *in–situ* scans illustrating the structural changes that $La_6W_2O_{15}$ undergoes by heating from 100 °C to 1100 °C recorded in steps of 50 °C and in the 2Theta range of 18 – 37.5°. Figure 3 (b) displays the top view onto the stack of scans recorded in the temperature range from 400 to 1100 °C and back to 400 °C in the 2Theta range from 26.4° to 35.4°.

The thermo–diffraction study showed that the low temperature phase γ –$La_6W_2O_{15}$ undergoes structural changes with increasing temperature. Applying cluster analysis (i.e. analysis of similarity) to the recorded scans at 25 °C and in the studied range of 100 – 1100 °C, four temperature ranges with relatively stable scans could be determined: 25 – 150 °C (*S1*), 400 – 600 °C (*S2*), 650 – 800 °C (*S3*), and 900 – 1100 °C (*S4*), indicating the existence of four stable structures referred as *S1* to *S4*.

Previously discussed structural transitions at about 600 °C (*S2*–to–*S3*) and 900 °C (*S3*–to–*S4*) correspond well to the earlier works (Ivanova *et al.* 1970, Chambrier *et al.* 2010). The transition from *S1* to *S2* over a metastable structure, existing in the temperature range of 150 – 400 °C, has no equivalent in the literature.

As seen from Figure 3, the reflections intensity does not change dramatically within the temperature ranges, indicated above. However, individual reflection groups do not behave equally with increasing temperature. Some of them shift towards the smaller Bragg angles, whereas others nearly do not change their positions or even move towards the larger Bragg angles. This different behaviour can be understood by an anisotropic thermal expansion of the unit cell. Each reflection represents a set of certain lattice planes. In dependence of their orientation in the unit cell, they reflect certain thermal expansion anisotropy. If a lattice plane distance increases with increasing temperature the corresponding reflection moves to lower Bragg angles, and vice versa.

Between the defined structural stability ranges, recorded reflections with strong intensity do not change considerably, while those with lower intensity disappear and later appear at different angle, indicating a partial atomic rearrangement. For example, the main peak of the reflection group at 34.5° shifts smoothly to the smaller Bragg angles, while the peak of higher intensity recorded at 28.7° remained unchanged with the temperature. We assume that the sublattices of heavy La^{3+}– and W^{6+}–ions (with corresponding strong intensity reflections) remain considerably stable, while oxygen and its rearrangements is responsible for the evidenced structural changes. The loss of oxygen with increasing temperature induces sublattice distortions and initiates structural transformations.

In Figure 3 (b), this anisotropic thermal expansion of the individual unit cells, together with the unit cell structure transformations, becomes very clear. While strong reflections exhibit rather smooth shifts (relatively stable sublattice(s) of heavy ions), low intensity reflections are shifted within the ranges of structural stability and change its position discontinuously in between.

In order to determine the microscopic thermal expansion coefficients, the most representative scan of each stability range were indexed using TOPAS 4.2 resulting in a space group and lattice parameters. These data were used in the next step to refine the lattice parameters of the unit cell by parametric Pawley refinement with TOPAS. Microscopic thermal expansion coefficients as a function of the crystallographic structure are presented in Figure 4. Results of the calculations are summarized in Table 1.

The orthorhombic symmetry remains in the entire temperature range. Between 700 and 850 °C the symmetry increases through face centring, which correlates with the maximum of microscopic thermal expansion coefficient due to the oxygen expelled from the lattice. The increased mobility of light species in the crystal lattice enables the geometric rearrangement of the heavier ones, as well.

Due to the identified structural changes and the pronounced thermal expansion anisotropy of the unit cell, the thermal treatment of $La_6W_2O_{15}$ usually results in an intensive crack formation, which cannot be controlled or

suppressed even by very slow heating and cooling rates. The structural transformations of this phase take place in the temperature range of membrane application. Therefore its presence in the LWO–membrane ought to be prevented.

3.2. Microstructural study

Figure 5 (a) presents a SEM micrograph of the unpolished surface of untreated $La_6W_2O_{15}$ sample, sintered at 1400 °C for 12h, while the micrographs in Figure 5 (b) and Figure 5 (c) show, respectively, the unpolished and polished surface of the sample after exposure to different gas environments, thermal cycles and voltage during the conductivity tests.

The as–sintered sample showed well shaped polygonal grains with an average size in the range from 3 to at least 10 µm. The low amount of isolated pores, which are randomly distributed, indicates optimal sintering. After exposing the sample to the conductivity test conditions for about 145 hours, followed by continuous thermal cycles in the range of 25 – 900 °C, particles a few µm in size can be observed, forming uneven surface (Figure 5 (b)).

Additionally, there is a number of cracks visible in Figure 5. The high crack density suggests strong thermo–mechanical stresses due to the polymorphism, which are especially intensive after the conductivity measurements (Figure 5 (c)).

The TEM study was carried out on cross sections of $La_6W_2O_{15}$ samples before (Figure 6 (a)) and after (Figure 6 (b) and (c)) the conductivity measurements, aiming to collect further evidence on the microstructural and functional degradation of the material. The sample surface was covered by protection layers added during the TEM–specimen preparation procedure. The cover layers are indicated on the micrographs.

As it can be seen from Figure 6 (a–c), clear difference in the surface (beneath the cover layers) quality before and after the tests can be observed, attributed to the microstructure degradation due to material operation under the respective test conditions.

In Figure 6 (a) crystal grains and cracks are clearly visible in the as–sintered specimen and no secondary phase was evidenced by the EDX. On the contrary, islands of precipitates can be observed on the treated sample surface, shown in Figure 6 (b), whereas the bulk remained unchanged. The area, indicated with a white rectangle in Figure 6 (b), is shown at higher magnification in Figure 6 (c), revealing a precipitate with inhomogeneous contrast.

The chemical composition at these degraded surface locations (the area in Figure 6 (c) marked with white circle) was analyzed by the EDX and the corresponding spectrum is shown in Figure 7 (a). For comparison, the EDX spectrum of the as–sintered bulk material is shown in Figure 7 (b).

Cu–lines in both spectra originate from the supporting net. The surface particles showed chemical composition corresponding to the following stoichiometry: La (20 at.%), Fe (10 at.%), O (65–70 at.%). Traces of sulphur of less than 2 % were found, as well. The elemental distribution in these particles is inhomogeneous, that makes difficult to ascertain a specific occurred phase.

The reason for the presence of iron in such an amount remains, however, unclear. In any case, it cannot be attributed to the raw materials quality. The impurities contained in the raw materials were analyzed by means of the LA–ICP–MS (Laser Ablation–Inductively Coupled Plasma–Mass Spectrometry) carried out by Agilent 7500ce at the Central Department of Chemical Analysis of the Research Centre Jülich. Iron in a concentration less than 77 ppm was detected for example in the WO_3, which oxide has lower purity than the La_2O_3. This amount is, however, much below the detected quantity in the post–treated sample, which is about 125 300 ppm.

3.3. Electrical conductivity study

3.3.1. Total conductivity as a function of temperature and gas environments

The total conductivity of $La_6W_2O_{15}$, measured as a function of temperature in (a) dry air and air saturated with H_2O, (b) dry Ar and Ar saturated with H_2O and (c) dry mixture of 4 % H_2 in Ar and when saturated with H_2O, is presented in Figure 8.

Two major trends were highlighted by these results and are discussed respectively here.

- *Conductivity–defects concentration correlation*

The total conductivity is higher in wet compared to dry atmospheres at low to intermediate temperatures (300 – 650 °C) as seen from Figure 8. This effect can be assigned to the material hydration, meaning that the protons contribute significantly to the total conductivity in the mentioned range. Figure S1 from the supporting section illustrates furthermore the predominant protonic contribution in the discussed temperature range. By comparing the conductivity data obtained for O_2 saturated with H_2O and D_2O, a clear isotope effect, which lays within the theoretical $\sqrt{2}$ value for the ratio $\sigma(H_2O/\ \sigma(D_2O)$, can be observed to about 630 °C (the temperature of the $\gamma-$ to$-\beta$ phase transition).

The most pronounced protonation effect at low temperatures was observed in Ar–atmosphere and it corresponds to a conductivity increase of at least one order of magnitude upon saturation with water. The conductivity becomes independent on water vapor pressure with further increase in the temperature and this trend holds true for all three atmospheres. In Ar, the difference in conductivity between dry and wet atmospheres vanishes at about 750–800 °C, whereas in air and 4% H_2 in Ar this effect can be observed at about 650 °C and 600 °C, respectively. The proton concentration decreases with increasing the temperature due to the exothermic nature of oxide hydration. However, the observed difference in the dehydration temperature as a function of the environment can be assigned to the proton defects concentration, which affects the dehydration temperature. This implies that the proton defects concentration decreases as the environment changes from wet Ar to wet air and, finally, to wet mixture of 4% H_2 in Ar, which is satisfied by the defect chemistry prediction. The electroneutrality condition in wet air or H_2–containing inert gas can be expressed as $[h^{\bullet}]+[OH^{\bullet}_O]=[e']$, meaning that in such conditions electron holes and the proton defects are charge compensating for defect electrons. In the case of Ar–atmosphere, saturated with H_2O, the electroneutrality requires that the condition $[2v^{\bullet\bullet}_O]+[OH^{\bullet}_O]=[e']$ is fulfilled. However, the oxygen vacancies are additionally hydrated that would increase the concentration of proton defects incorporated in the lattice.

Figure 9 shows the total conductivity of $La_6W_2O_{15}$ measured as a function of the oxygen partial pressure in a *log–log* plot under dry conditions at various temperatures.

The following equations in Kröger–Vink notations describe the two boundary conditions:

Dry oxidizing conditions:

$$\frac{1}{2}O_{2(gas)} + v^{\bullet\bullet}_O \rightarrow O^X_O + 2h^{\bullet} \tag{2a}$$

$$K_p = \frac{[O^X_O][h^{\bullet}]^2}{[v^{\bullet\bullet}_O]p^{1/2}_{O2}} \tag{2b}$$

$$[h^{\bullet}] \propto (p_{O2})^{1/4} \tag{2c}$$

Dry reducing conditions:

$$O^X_O \rightarrow v^{\bullet\bullet}_O + 2e' + \frac{1}{2}O_2 \tag{3a}$$

$$K_n = \frac{[v^{\bullet\bullet}_O][e']^2 p_{O2}{}^{1/2}}{[O^X_O]} \tag{3b}$$

$$[e'] \propto (p_{O2})^{-1/4} \tag{3c}$$

The obtained experimental results, plotted in Figure 9, are in a good agreement with the defect chemical model, according to which $La_6W_2O_{15}$ exhibits conductivity of *n*–type, when exposed to low p_{O2} – environments (Eq. 3). The observed dependence holds true within the whole temperature range and the slope of ($-1/4$) is a clear indication for that. Although the slope deviates from the predicted value at lower temperatures (300 °C), the conductivity of $La_6W_2O_{15}$ is not entirely independent on the p_{O2}, meaning that $La_6W_2O_{15}$ is essentially a mixed electronic–ionic conductor in dry atmospheres and in the tested range of p_{O2}. In oxidizing conditions, the electron holes also start to contribute to the conductivity (Eq. 2). However, this effect is less pronounced for the corresponding set of experimental conditions.

The relatively low activation energies for conductivity obtained in the temperature range 300 – 600 °C (see Figure 8 and Figure S2), might be assigned to the electronic conductivity under dry conditions (0.10 – 0.15 eV), as shown in Figure 9, and to the protonic or mixed protonic–electronic conductivity under wet conditions (0.15 – 0.20 eV), as defined by the defect–chemical model regarded above and supported by the experimental data in Figure 8, respectively. Furthermore, considering the significant contribution of the oxygen ions at elevated temperatures, the higher activation energies above 600 °C (to about 0.85 eV for dry atmospheres) might be referred to the oxygen ion mobility, which is normally assigned to the high activation enthalpies. Nevertheless, it is difficult to ascertain the relative contributions of different charge carriers with reaction conditions, but possibly expected pressure dependencies might be deduced for given electroneutrality conditions. In any case, no pronounced differences in the activation energies with the tested gas conditions were found for the two temperature ranges (300 – 600 °C and 600 – 900 °C) of consideration. Therefore, apart from the defect thermodynamics, another aspect related to the structural features of the material and the local arrangements in vicinity to the incorporated protons may come into play, when data are interpreted.

- *Conductivity–structure correlation*

As seen in Figure 8, and additionally Figure S1, the conductivity does not follow the typical Arrhenius behavior $\log(\sigma) \propto 1/T$ over the entire range of temperatures. Two linear ranges may be recognized with transition temperature of about 600 °C and regardless to the experimental gas atmosphere. This behavior can be ascribed both to *i)* the change in the dominant charge carrier concentrations and respectively, the conduction mechanism, as a function of the temperature and *ii)* the phase transition that takes place at nearly the same temperature, as shown in the structural part of the present paper and previously described in (Ivanova *et al.* 1970, Yoshimura *et al.* 1976, Chambrier *et al.* 2010). The second phase transition, which takes place at temperatures higher than 900 °C and leads to the high–temperature α –polymorph, cannot be visualized in the present conductivity plots due to the limitation in the temperature range.

As previously discussed, the gradual de–protonation of the oxide with the temperature, which was evidenced by decreasing proton conductivity, and the dominant role of the oxygen ions and electrons at higher temperatures, as evidenced by the higher thermal activation, are reflected by point *i)*. The fact that the activation energies for conductivity in all dry atmospheres have very close values, and the same holds true for the set of measurements carried out in wet atmospheres, supports this observation.

The second point *ii)* reflects the fact that the conductivities measured in the lower temperature range and associated with relatively low activation energies (0.10 – 0.20 eV) correspond to the low temperature polymorph, referred as the γ –form. Consecutively, the upper temperature range corresponds to the β–$La_6W_2O_{15}$ and related conductivities are associated with higher activation energies (0.55 – 0.85 eV).

As discussed by Kreuer (Kreuer 2003), in the light of the hydrogen bond thermodynamics, an activation enthalpy of long–range diffusion of not more than 0.15 eV might be expected (that suggests linear configuration O–H...O, as well as O–O separation less than ~2.5 Å). The data obtained in the present study for wet or H_2–containing atmospheres in the lower temperature range (300 – 600 °C) are therefore in a good agreement with the considered literature data. Activation enthalpies for proton mobility ranging from 0.4 to 0.6 eV were determined for the cubic perovskites [53] due to the contribution of other complex interactions not discussed here.

Furthermore, according to (Chambrier *et al.* 2010), the proposed structural model for the high temperature α –form, usually existing above 900 °C, can be adopted by the two other polymorphs based on similarity.

Therefore, the present conductivity data are regarded in terms of the structural features of the only studied and modeled α –form.

As the structural model describes, the α –structure comprises ordered [La–O]–motifs, forming double ribbons $(La_3O_2)_\infty$, as well as disordered $[WO_{5.5}]$–tetrahedra, leading to $[La_3O_2]_2[WO_{5.5}]_2$ as a general formula of the compound. Furthermore, the La–O interatomic bond distances range from ~2.3 to ~3 Å and are larger than the W–O distances (ca. 1.7 – 1.9 Å). The $[W_2O_{11}]$–unit must fit in one crystallographic site, thus implying disorder and possible origin of the phase transition, while at lower temperatures non–equivalent W–atomic positions may be adopted leading to ordering of the structure. Furthermore, the $[W_2O_{11}]$ – entity is formed by two corner–sharing $[WO_6]$–octahedra with a distance between the two W–atoms equal to 4.13 Å. However, when the distance d(W–W) increases, disorder is induced, as in the case of the $[WO_{5.5}]_2$–units having d(W–W) of 5.55 Å (Chambrier *et al.* 2010).

In the light of the findings for the cubic perovskites (Kreuer 1999, Kreuer 2003), and for the α –polymorph (Chambrier *et al.* 2010), we propose that *1)* the protons, incorporated in the crystal lattice, are preferentially allocated in proximity to the [W–O] structural units, thus affecting the W–W distance and possibly inducing ordering; and *2)* the proton mobility paths are allocated in the vicinity of the W–atoms due to the shorter W–O distance. In this context, it is remarkable that the activation energy change is less abrupt when water is present in the surrounding atmosphere (Figure S3 (b)). This effect can be eventually assigned to the local structural re–arrangement or relaxations, introduced by the protonation of the oxide. The incorporation of protons could possibly "stabilize" the [W–O] structural motifs and the sharp γ – to β –polymorph transition might be affected indeed. With increasing temperature the structure dehydrates, but this process has a gradual character, therefore the break around the temperature of polymorph transition is not as sharp as in dry atmospheres. However, these suggestions will need further experimental support by e.g. HT–XRD studies in wet atmosphere to elucidate the role of water on the structure and polymorphism of $La_6W_2O_{15}$, as well as atomistic modeling to clarify the proton positions and the proton mobility paths.

3.3.2. Conductivity relation between $La_6W_2O_{15}$ and $La_{6-x}WO_{12-\delta}$

The total *ac*–conductivity of $La_6W_2O_{15}$ was compared to that of LWO, both measured as a function of the inverse temperature in different atmospheres (Figure 10). This comparison aims to illustrate the influence of the orthorhombic $La_6W_2O_{15}$ phase on the electrical properties of the LWO main phase. The frequency value was fixed at about 12 kHz for giving an insight into the bulk conductivity of the two materials.

As it can be inferred from the figure, the two tested materials exhibit close conductivity values at 900 °C. Nevertheless, in the low to intermediate temperature range (300 – 650 °C), the observed difference in the conductivities became larger and extends over two orders of magnitude, with higher values measured for the LWO compound.

Therefore, it can be concluded that the presence of the $La_6W_2O_{15}$ compound as a secondary phase in the LWO–based membranes or components will affect negatively the overall electrical conductivity, apart from the microstructural and thermal drawbacks, as discussed in the previous sections.

3.3.3. Conductivity relaxation study

The oxidation and hydration kinetics have been studied by conductivity relaxation upon stepwise changes in the oxygen or water vapour activities, aiming to analyze diffusion (D) and surface exchange coefficients (k) of $La_6W_2O_{15}$ in a hydration process. A number of proton conductors such as $SrCe_{0.95}Yb_{0.05}O_{2.975}$ (Yoo *et al.* 2008), doped $SrZrO_3$ (Kudo *et al.* 2008), doped $BaTiO_3$ (Song *et al.* 2000) and LWO (Solís *et al.* 2011) were similarly studied.

Figure 11 (a) shows the *dc*–conductivity at 450 °C as a function of time upon a change from dry to wet air.

It can be observed that the conductivity increases, when the atmosphere is humidified, due to the protonic transport and it follows a single–fold monotonic behavior with one diffusion coefficient.

A similar behavior, ascribed to the ambipolar water diffusion, was reported for $La_{5.5}WO_{12-\delta}$ compound (Solís *et al.* 2011). The obtained curve can be fitted to the analytic solution of Fick's second law. For a rectangular

bar ($2l_x$ x $2l_y$ x $2l_z$) it can be described with Eq. 4, according to (Song *et al*. 1999, Søgaard *et al.* 2007), where σ is the total conductivity as a function of time, σ_0 and σ_∞ are the conductivities at time zero and infinitum, respectively.

$$\frac{\sigma-\sigma_0}{\sigma_\infty-\sigma_0}=1-\left[\sum_{n=1}^{\infty}\frac{2L_x^2}{\beta_{n,x}^2\left(\beta_{n,x}^2+L_x^2+L_x\right)}\exp\left(\frac{-\beta_{n,x}^2 Dt}{l_x^2}\right)\sum_{m=1}^{\infty}\frac{2L_y^2}{\beta_{m,y}^2\left(\beta_{m,y}^2+L_y^2+L_y\right)}\right.$$

$$\left.\exp\left(\frac{-\beta^2{}_{m,y}Dt}{l_y^2}\right)\sum_{m=1}^{\infty}\frac{2L_z^2}{\beta_{m,z}^2\left(\beta_{m,z}^2+L_z^2+L_z\right)}\exp\left(\frac{-\beta_{m,z}^2 Dt}{l_z^2}\right)\right] \quad (4)$$

$$\text{with}\quad L_i=\beta_{n,i}\tan\beta_{n,i}\equiv\frac{l_i k}{D}\quad,\quad i=x,y,z$$

Coefficients D and k obtained from the fitting of the hydration transients from 450 to 750 °C are shown in Figure 11 (b) as a function of the inverse temperature. It can be observed that the diffusion coefficients in air are in the range $4\cdot10^{-4}$ – $7\cdot10^{-6}$ $cm^2\cdot s^{-1}$ from 450 to 750 °C, which has similar magnitude as the coefficients previously reported for other proton conductors (Yoo *et al.* 2009). Surface exchange coefficients range between $1\cdot10^{-3}$ – $2\cdot10^{-2}$ $cm\cdot s^{-1}$ and these values are similar to other oxygen ion conductions (Preis *et al.* 2004). Furthermore, a possible change in the activation energy of D at around 650 °C (not observed for k) can be associated with the structural change around that temperature. This fact evidences unambiguously the direct impact of the phase transition on the ionic transport (Solís *et al.* 2011). Moreover, activation energies for diffusion in the range of 0.55 – 1.59 eV are very similar to those, reported previously for oxygen and oxygen vacancies (Kreuer *et al.* 1994).

Consequently, together with the single–fold monotonic behavior of relaxation, the two coefficients, k and D, reflect migration of charge carriers not related with protons/deuterons, e.g. oxygen vacancies/oxygen ions through the polycrystalline oxide. Furthermore, the hydration process in $La_6W_2O_{15}$ phase was found to be faster compared to the LWO phase (Solís *et al.* 2011), possibly due to the higher electronic contribution to the total conductivity of $La_6W_2O_{15}$.

3.4. Chemical compatibility of $La_6W_2O_{15}$ with conventional substrate materials

In terms of several industrial applications, a better membrane performance can be achieved when the membrane thickness is decreased, usually by fabrication of functional layer on a suitable porous substrate. Therefore, the chemical compatibility of the $La_6W_2O_{15}$ with substrate materials was tested.

Materials selected for the compatibility experiment were NiO, YSZ and CGO used in the conventional SOFC technology, in addition to the MgO as a possible substrate solution in the manufacturing of supported membranes for gas separation. Table 2 summarizes the conditions and products of the corresponding reactions. Diffraction patterns of the reaction products of $La_6W_2O_{15}$ with a) CGO; b) YSZ; c) NiO and d) MgO at 800 °C/12h and 1400 °C/12h are presented in Figure S4.

Results clearly showed that the $La_6W_2O_{15}$ did not form any reaction products with CGO and MgO within the whole tested temperature range, as well as with YSZ at 800 °C and 1000 °C. At 1400 °C, $La_6W_2O_{15}$ and YSZ form a pyrochlore–structured compound $La_2Zr_2O_7$ (PDF 01–071–2363), as well as $La_2W_2O_9$ (PDF 00–034–0704) (Ivanova *et al.* 1970, Yoshimura *et al.* 1976, Marrero–Lopez *et al.* 2008). With NiO there was no reaction detected at 800 °C, whereas at T ≥ 1000 °C, the orthorhombic phase $LaNi_{0.8}W_{0.2}O_3$ (PDF 01–086–1178) was formed. Similar reaction products and temperatures were reported for Nd_6WO_{12} (NdWO) (Escolástico *et al.* 2009). A recent study on the compatibility of LWO with the same substrate materials carried out in our Labs (Seeger, Ivanova *et al.*: article in preparation) evidenced identical reactivity issues. Therefore, when present as a secondary phase in the LWO–based membrane, $La_6W_2O_{15}$ will not affect considerably the chemical compatibility of LWO with the tested variety of substrate materials.

3.5. Chemical stability of the $La_6W_2O_{15}$ compound in reducing atmospheres

H_2–separating dense ceramic membranes need to exhibit significant chemical stability at elevated temperatures, especially in humid reducing atmospheres and CO_2–rich environment. Certain membrane materials, e.g. cerate–based, suffer from insufficient stability induced by carbonation, hydroxide formation, and reduction when exposed to the above mentioned conditions, leading to mechanical and functional degradation.

In order to estimate the short–term chemical stability of $La_6W_2O_{15}$ and its influence on the LWO–based membrane, tests were carried out in: *(1)* wet (2.5 vol.% H_2O) gas flow of 10% CO_2 in CH_4 at 750 °C for 72 h, and *(2)* wet (2.5 vol.% H_2O) flow of 100 vol.% H_2 at 900 °C for 55 h. These environments were selected to simulate the conditions of H_2/CO_2 separation using a dense ceramic membrane. With respect to the carbonation test, temperature of 750 °C is high enough for carbonation evolution, but below carbonate decomposition (Jeevanadam *et al.* 2001, Escolástico *et al.* 2009).

Figure 12 displays the XRD patterns of $La_6W_2O_{15}$ recorded for a fresh sample after sintering and for samples exposed to the two corresponding sets of experimental conditions.

It can be clearly observed from the figure that no new phases appear. This result demonstrates that $La_6W_2O_{15}$ remains stable to carbonation and reduction in the selected experimental window by analogy to NdWO (Escolástico *et al.* 2009) and LWO (Seeger, Ivanova *et al.*: article in preparation). Therefore, it may be concluded that the stability of LWO–based membrane will not be affected by instabilities of the $La_6W_2O_{15}$ secondary phase under the considered conditions.

4. Conclusion

Single phase $La_6W_2O_{15}$ material was synthesized via the conventional solid state route from stoichiometric amounts of constituent oxides. Investigation on the crystal lattice structure over the temperature was carried out in the range from room temperature up to 1100 °C both in a heating and cooling mode. Four stable structures were detected in the studied temperature range, one having no analogue in the literature. These structural transformations were found to be associated with strong variations in the microscopic thermal expansion coefficients. As a result, internal tensions are accumulated in the material, leading to cracked microstructure, as evidenced by the electron microscopy. Apart from the negative microstructural influence, the presence of $La_6W_2O_{15}$ was identified as disadvantageous also for the electrical properties of LWO membrane. The conductivity measurements performed for $La_6W_2O_{15}$ and LWO at similar experimental conditions showed that the electrical conductivity of $La_6W_2O_{15}$ was several orders of magnitude lower than that of the LWO, especially in the low to intermediate temperature range. The secondary phase exhibits proton conductivity in humid atmospheres as evidenced by the electrical characterization and conductivity relaxation study, while at low p_{O2} electronic and mixed conductivity dominates. Surface exchange and diffusion coefficients have been determined by means of conductivity relaxation study, showing that the hydration of the $La_6W_2O_{15}$ phase is faster than in the LWO phase. The presence of the $La_6W_2O_{15}$ is not expected to affect the chemical compatibility of LWO with various standard substrate materials due to the similarities in the reaction behaviour of the two compounds. $La_6W_2O_{15}$ demonstrated short term stability against carbonation and reduction when exposed to simulated H_2/CO_2 separation conditions, hence the stability of LWO–membrane under similar conditions will not be affected by the secondary phase $La_6W_2O_{15}$.

References

Amezawa, K.; Kjelstrup, S.; Norby, T.; Ito, Y. (1998). Protonic and native conduction in Sr–substituted $LaPO_4$ studied by thermoelectric power measurements. *J. Electrochem. Soc.* 145, 3313–3319.

Amezawa, K.; Kitajima, Y.; Tomii, Y.; Yamamoto, N. (2004). High–temperature protonic conduction in LaP_3O_9. *Electrochem. Solid State Lett.* 7, A511–A514.

Balakrieva, V.B.; Gorelov, V.P. (1989). Proton and hole transport in CaO–doped erbia. *Solid Stale Ionics* 36, 217–218.

Brandão, A.D.; Gracio, J.; Mather, G.C.; Kharton, V.V.; Fagg, D.P. (2011). B–site substitutions in

$LaNb_{1-x}M_xO_{4-\delta}$ materials in the search for potential proton conductors (M=Ga, Ge, Si, B, Ti, Zr, P, Al). *J. Solid State Chem.* 184, 863–870.

Chambrier, M.H.; Ibberson, R.M.; Goutenoire, F. (2010). Structure determination of α–$La_6W_2O_{15}$. *J. Solid State Chem.* 183, 1297–1302.

Chang, L.L.Y.; Phillips, B. (1964). Samarium and lanthanum tungstates of the $3R_2O_3.WO_3$ type. *Inorg. Chem.* 3, 1792–1794.

Czyperek, M.; Zapp, P.; Bouwmeester, H.J.M.; Modigell, M.; Ebert, K.; Voigt, I.; Meulenberg, W.A.; Singheiser, L.; Stöver, D. (2010). Gas separation membranes for zero–emission fossil power plants: MEM–BRAIN. *J. Mem. Sci.* 359, 149–159.

Escolástico, S.; Vert, V.B.; Serra, J.M. (2009). Preparation and characterization of nanocrystalline mixed proton–electronic conducting materials based on the system Ln_6WO_{12}. *Chem. Mater.* 21, 3079–3089.

(a) Escolástico, S.; Solis, C.; Serra, J.M. (2011). Study of hydrogen permeation in $(La_{5/6}Nd_{1/6})_{5.5}WO_{12-\delta}$ membranes. *Solid State Ionics*, article in press.

(b) Escolástico, S.; Solis, C.; Serra, J.M. (2011). Hydrogen separation and stability study of ceramic membranes based on the system Nd_5LnWO_{12}. *Intl. J. Hydrogen Energy* 36, 11946–11954.

(a) Eurenius, K.E.J.; Ahlberg, E.; Ahmed, I.; Eriksson, S.G.; Knee, C.S. (2010). Investigation of proton conductivity in $Sm_{1.92}Ca_{0.08}Ti_2O_{7-\delta}$ and $Sm_2Ti_{1.92}Y_{0.08}O_{7-\delta}$ pyrochlores. *Solid State Ionics* 181, 148–153.

(b) Eurenius, K.E.J.; Ahlberg, E.; Knee, C.S. (2010). Proton conductivity in $Sm_2Sn_2O_7$ pyrochlores. *Solid State Ionics* 181, 1577–1585.

Fontaine, M.L.; Larring, Y.; Norby, T.; Grande, T.; Bredesen, R. (2007). Dense ceramic membranes based on ion conducting oxides. *Ann. Chim. Sci. Mat.* 32, 197–212. –

Gorelov, V.P.; Balaklreva, V.B. Izv. Akad. Nauk. SSSR, (1990). *Inorg. Mat.* 26, 102.

Haugsrud, R.; Norby, T. (2005). In Proceedings of the 26th Risø International Symposium on Materials Science: Solid State Electrochemistry, Linderoth, S.; Smith, A.; Bonanos, N.; Hagen, A.; Mikkelsen, L.; Kammer, K.; Lybye, D.; Hendriksen, P.V.; Poulsen, F.W.; Mogensen, M.; Wang, W.G.; Ed.; Risø National Laboratory, Roskilde, DK.

(a) Haugsrud, R.; Norby, T. (2006). Proton conduction in rare–earth ortho–niobates and ortho–tantalates. *Nat. Mater.* 5, 193–196.

(b) Haugsrud, R.; Norby, T. (2006). High–temperature proton conductivity in acceptor–doped $LaNbO_4$. *Solid State Ionics* 177, 1129–1135.

(a) Haugsrud, R.; Norby, T. (2007). Proton conductivity in acceptor substituted $LnTaO_4$. *J. Am. Ceram. Soc.* 90, 1116–1121.

(b) Haugsrud, R. (2007). Defects and transport properties in Ln_6WO_{12} (Ln = La, Nd, Gd, Er). *Solid State Ionics* 178, 555–560.

Haugsrud, R.; Kjølseth, C. (2008). Effects of protons and acceptor substitution on the electrical conductivity of La_6WO_{12}. *J. Phys. Chem. Sol.* 69, 1758–1765.

Huse, M.; Norby, T.; Haugsrud, R. (2012). Effects of A and B site acceptor doping on hydration and proton mobility of $LaNbO_4$. *Intl. J. Hydrogen Energy*, article in press.

(a) Ivanova, M.E.; Ricote, S.; Baumann, St.; Meulenberg, W.A.; Tietz, F.; Serra, J.M.; Richter, H. (2012). Ceramic materials for energy and environmental applications: functionalizing of properties by tailored compositions in *Doping: Properties, Mechanisms and Applications*, NOVA Science Publishers Inc., NY, USA, Chapter in press.

(b) Ivanova, M.E.; Ricote, S.; Meulenberg, W.A.; Haugsrud, R.; Ziegner, M. (2012). Effects of A– and B–site (co–)acceptor doping on the structure and proton conductivity of $LaNbO_4$. *Solid State Ionics* 213, 45–52. doi:10.1016/j.ssi.2011.06.012.

Ivanova, M.M.; Balagina, G.; YaRode, E. (1970). Izv. Akad. Nauk SSSR, *Neorg. Mater.* 6, 914.

Jeevanadam, P.; Koltypin, Yu.; Palchik, O.; Gedanken, A. (2001). Synthesis of morphologically controlled lanthanum carbonate particles using ultrasound irradiation. *J. Mater. Chem.* 11, 869–873.

Jordal, K.; Bredesen, R.; Kvamsdal, H.M.; Bolland, O. (2004). Integration of H_2–separating membrane technology in gas turbine processes for CO_2 capture. *Energy* 29, 1269–1278.

Kreuer, K.D.; Schönherr, E.; Maier, J. (1994). Proton and oxygen diffusion in $BaCeO_3$, based compounds: a combined thermal gravimetric analysis and conductivity study. *Solid State Ionics* 70/71, 278–284.

Kreuer, K.D. (1999). Aspects of the formation and mobility of protonic charge carriers and the stability of perovskite–type oxides. *Solid State Ionics*, 125, 285–302.

Kreuer, K.D. (2003). Proton–conducting oxides. *Annu. Rev. Mater. Res.* 33, 333–359.

Kudo, T.; Yashiro, K.; Matsumoto, H.; Sato, K.; Kawada, T.; Mizusaki, J. (2008). Slow relaxation kinetics of $Sr(Zr,Y)O_3$ in wet atmosphere. *Solid State Ionics* 179, 851–854.

Larring, Y.; Norby, T. (1995). Protons in rare earth oxides. *Solid State Ionics* 77, 147–151.

Larring, Y.; Norby, T. (1997). The equilibrium between water vapour, protons, and oxygen vacancies in rare earth oxides. *Solid State Ionics* 97, 523–528.

Li, L.; Borry, R.W.; Iglesia, E. (2002). Design and optimization of catalysts and membrane reactors for the non–oxidative conversion of methane. *Chem. Eng. Sci.* 57, 4595–4604.

Magrasó, A.; Frontera, C.; Marrero–López, D.; Nuñez, P. (2009). New crystal structure and characterization of lanthanum tungstates "La_6WO_{12}" prepared by freeze–drying synthesis. *Dalton Trans.* 10273–10283.

Marrero–Lopez, D.; Pena–Martinez, J.; Ruiz–Morales, J.C.; Nunez, P. (2008). Phase stability and ionic conductivity in substituted $La_2W_2O_9$. *J. Solid State Chem.* 181, 253–262.

Mc Carthy, G.J.; Fischer, R.D.; Johnson Jr., G.G.; Gooden, C.E. (1972). *NBS Special Publication: Solid State Chemistry*, 364, 397.

Meulenberg, W.A.; Ivanova, M.E.; van Gestel, T.; Bram, M.; Buchkremer, H.P.; Stöver, D.; Serra, J.M. (2010). State of the art of ceramic membranes for hydrogen separation. In *Hydrogen and Fuel Cells*, Edt. Stolten, D., Wiley–VCH Verlag, Weinheim, ISBN: 978–3–527–32711–9, 321–349 (Chapter 16).

Meulenberg, W.A.; Ivanova, M.E.; Roitsch, St.; Serra, J.M. (2011). Proton–conducting ceramic membranes for solid oxide fuel cells and hydrogen (H_2) processing. In *Advanced membrane science and technology for sustainable energy and environmental applications*, Part IV Membranes for alternative energy applications: batteries, fuel cells and hydrogen (H_2) production, Edts: Angelo Basile, Suzana Pereira Nuñes, Woodhead Publishing Series in Energy №25, Woodhead Publishing Limited, Cambridge, UK, ISBN 978–1–84569–969–7, 541–567 (Chapter 17).

Mokkelbost, T.; Kaus, I.; Haugsrud, R.; Norby, T.; Grande, T.; Einarsrud, M.A. (2008). High–temperature proton–conducting lanthanum ortho–niobate–based materials. Part II: sintering properties and solubility of alkaline earth oxides. *J. Am. Ceram. Soc.* 91, 879–886.

Norby, T.; Kofstad, P. (1984). Electrical conductivity and defect structure of Y_2O_3 as a function of water vapor pressure. *J. Am. Ceram. Soc.* 67, 786–792.

Norby, T.; Kofstad, P. (1986). Proton and native–ion conductivities in Y_2O_3 at high temperatures. *Solid State Ionics* 20, 169–184.

Norby, T. (1988). EMF method determination of conductivity contributions from protons and other foreign ions in oxides. *Solid State Ionics* 28–30, 1586–1591.

(a) Norby, T.; Dyrlie, O.; Kofstad, P. (1992). Protonic conduction in acceptor–doped cubic rare–earth sesquioxides. *J. Am. Ceram. Soc.* 75, 1176–1181.

(b) Norby, T.; Dyrlie, O.; Kofstad, P. (1992). Protons in Ca–doped La_2O_3, Nd_2O_3 and $LaNdO_3$. *Solid State Ionics* 53–56, 446–452.

Norby, T.; Christiansen, N. (1995). Proton conduction in Ca– and Sr–substituted $LaPO_4$. *Solid State Ionics* 77, 240–243.

(a) Norby, T.; Haugsrud, R. (2006). Dense ceramic membranes for hydrogen separation. In *Nonporous Inorganic Membranes,* Edt. Sammels, A.; Mundschau, M. Wiley–VCH Verlag GmbH & Co. KgaA, Weinheim, ISBN: 3–527–31342–7, 1–48 (Chapter 1).

(b) Norby, T.; Haugsrud, R.; Marion, St.; Einarsrud, M.A.; Wiik, K.; Andersen, Oy.; Strom, R.A.; Grande, T. (2006). Proton Conductors, *Patent* WO 2006/066918 A2.

Norby, T.; Haugsrud, R. (2007). High temperature proton conducting materials for H_2–separation. Invited lecture at FZJ Workshop, Jülich, DE, 16 November 2007.

Omata, T.; Okuda, K.; Tsugimoto, S.; Otsuka–Matsuo–Yao, S. (1997). Water and hydrogen evolution properties and protonic conducting behaviors of Ca^{2+}–doped $La_2Zr_2O_7$ with a pyrochlore structure. *Solid State Ionics* 104, 249–258.

Omata, T.; Ikeda, K.; Tokashiki, R.; Otsuka–Yao–Matsuo, S. (2004). Proton solubility for $La_2Zr_2O_7$ with a pyrochlore structure doped with a series of alkaline–earth ions. *Solid State Ionics* 167, 389–397.

Preis, W.; Bucher, E.; Sitte, W. (2004). Oxygen exchange kinetics of $La_{0.4}Sr_{0.6}FeO_{3-\delta}$ by simultaneous application of conductivity relaxation and carrier gas coulometry. *Solid State Ionics* 175, 393–397.

Serra, J.M.; Escolástico, S.; Ivanova, M.E.; Meulenberg, W.A, Buchkremer, H.P.; Stöver, D. (2012). CO_2 tolerant mixed conducting oxide and use thereof for hydrogen separation. *Patent* WO 2012/010386 A1.

Shimura, T.; Komori, M.; Iwahara, H. (1996). Ionic conduction in pyrochlore–type oxides containing rare earth elements at high temperature. *Solid State Ionics* 86–88, 685–689.

Shimura, T.; Fujimoto, S.; Iwahara, H. (2001). Proton conduction in non–perovskite–type oxides at elevated temperatures. *Solid State Ionics* 143, 117–123.

Søgaard, M.; Hendriksen, P.V.; Mogensen, M. (2007). Oxygen nonstoichiometry and transport properties of strontium substituted lanthanum ferrite. *J. Solid State Chem.* 180, 1489–1503.

Solís, C.; Escolástico, S.; Haugsrud, R.; Serra, J.M. (2011). $La_{5.5}WO_{12-\delta}$ Characterization of transport properties under oxidizing conditions: a conductivity relaxation study. *J. Phys. Chem. C*, 115, 11124–11131. dx.doi.org/10.1021/jp2015066.

Song, C.R.; Yoo, H.I. (1999). Chemical diffusivity of $BaTiO_{3-\delta}$: III. Conductivity–nonstoichiometry (δ) correlation in a mixed n/p regime. *Solid State Ionics* 124, 289–299.

Song, C.R.; Yoo, H.I. (2000). Chemical diffusivity of $BaTiO_{3-\delta}$: IV, acceptor–doped case. *J. Am. Ceram. Soc.* 83, 773–779.

Yoo, H.I.; Yoon, J.Y.; Ha, J.S.; Lee, C.E. (2008). Hydration and oxidation kinetics of a proton conductor oxide, $SrCe_{0.95}Yb_{0.05}O_{2.975}$. *Phys. Chem. Chem. Phys.* 10, 974–982.

Yoo, H.I.; Lee, C.E. (2009). Conductivity relaxation patterns of mixed conductor oxides under a chemical potential gradient. *Solid State Ionics* 180, 326–337.

Yoshimura, M.; Baumard, J.F. (1975). Electrical conductivity of solid solutions in the system CeO_2–La_6WO_{12}. *Mater. Res. Bull.* 10, 983–988.

Yoshimura, M.; Rouanet, A. (1976). High temperature phase relation in the system La_2O_3–WO_3. *Mat. Res. Bull.* 11, 151–158.

Notes

Note 1. Note that according to Ivanova *et al.* (Ivanova *et al.* 1970) the high temperature phase was referred as "γ", whereas Chambrier *et al.* (Chambrier *et al.* 2010) refers to it as "α". In the present work the notation according to Chambrier *et al.* was used.

Note 2. Crystal lattice parameters, given in Table 1, correspond to the underlined value of temperature.

Mariya E. Ivanova obtained her PhD in Materials Science and Engineering in 2008. Since then, she works as a researcher in the field of materials and membranes for energy and environmental applications at the Institute of Energy and Climate Research IEK–1, Forschungszentrum Jülich GmbH, Germany. Part of her previous studies was dedicated to the development of zeolite materials for catalytic membrane reactors and was carried out at the Institute of Membrane Technologies ITM–CNR (University of Calabria) headed by Prof. Enrico Drioli. Currently, her research activities are focused on the development of different kinds of functional oxides for proton–conducting SOFCs and H_2–separating membranes with an accent on functionalizing their properties by tailored compositions.

Table 1. Space groups, lattice parameters and thermal expansion coefficients (TECs) determined for $La_6W_2O_{15}$ from the HT–XRD study.

	Structure 1 (S1)	Structure 2 (S2)	Structure 3 (S3)	Structure 4 (S4)
Temp. range: (Note 2)	25–150 °C	400–600 °C	650 (700)–800 °C	900 (950)–1100 °C
Crystal class:	orthorhombic	orthorhombic	orthorhombic	orthorhombic
Space group:	C2221	C2221	F222	C2221
Lattice parameters				
a_{To} (Å)	17.881(2)	17.927(2)	25.441(1)	12.642(1)
b_{To} (Å)	25.483(3)	25.375(1)	18.251 (1)	9.219(1)
c_{To} (Å)	35.665(4)	35.817(2)	11.766(1)	5.992(1)
TEC				
α_a ($10^{-6}\cdot K^{-1}$)	5.0	17.2(7)	-3.3(3)	-9.3(3)
α_b ($10^{-6}\cdot K^{-1}$)	14.0	11.8	18.6(3)	18.7(3)
α_c ($10^{-6}\cdot K^{-1}$)	12.5	12.2(5)	46.0(3)	34.4(3)
$\alpha_{average}$ ($10^{-6}\cdot K^{-1}$)	10.5	13.7	20.4	14.6

Table 2. Conditions and products of the chemical reactivity of $La_6W_2O_{15}$ with CGO, YSZ, NiO and MgO used as substrate materials in the supported membrane manufacturing.

Powder mixture	Heat treatment		
	800 °C, 12 h	1000 °C, 12 h	1400 °C, 12 h
$La_6W_2O_{15}$ + CGO	No reaction	No reaction	No reaction
$La_6W_2O_{15}$ + YSZ	No reaction	No reaction	$La_2Zr_2O_7$ $La_2W_2O_9$
$La_6W_2O_{15}$ + NiO	No reaction	$LaNi_{0.8}W_{0.2}O_3$	$LaNi_{0.8}W_{0.2}O_3$
$La_6W_2O_{15}$ + MgO	No reaction	No reaction	No reaction

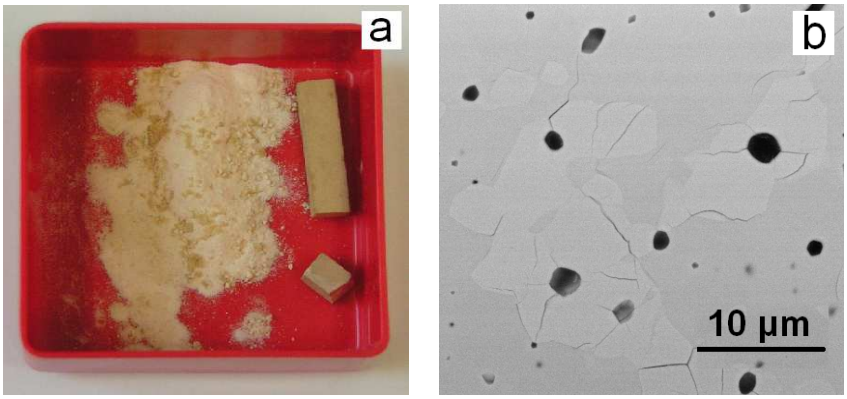

Figure 1. (a) Photograph of LWO bars sintered at 1450 °C for 24 h in air. The pulverization of the specimen was observed after several hours in atmospheric air due to the free La_2O_3 contained as a secondary phase; (b) Micrograph of a LWO membrane sintered at 1450 °C for 24 h in air. The cracks are located in the bright phase, identified via the EDX as the secondary phase $La_6W_2O_{15}$.

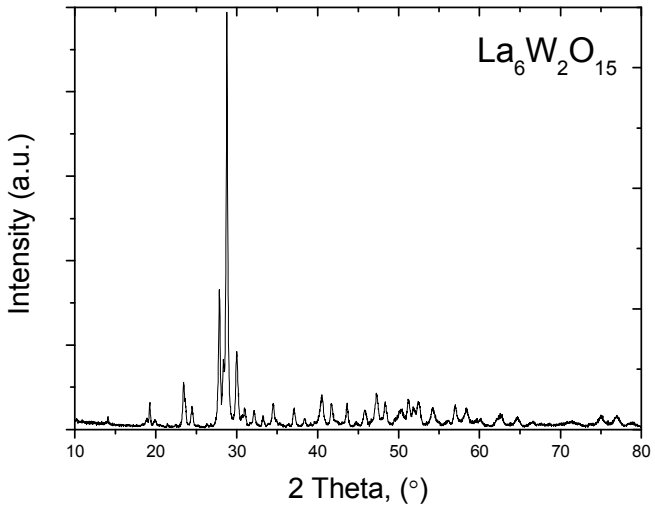

Figure 2. Diffraction pattern of $La_6W_2O_{15}$ powder after the solid state synthesis at 1000 °C/12h in air.

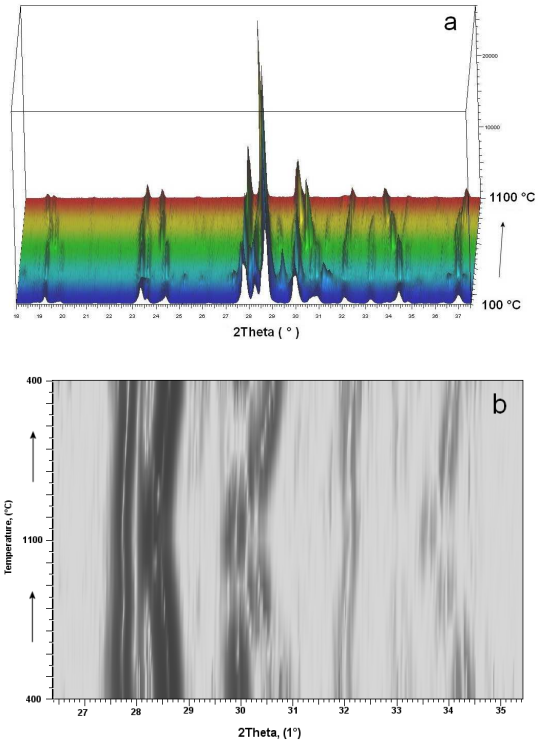

Figure 3. Thermo–diffraction patterns for $La_6W_2O_{15}$ recorded in: (a) a heating mode in the temperature range of 100 – 1100 °C and 2 Theta range from 18° to 37.5° as stacked patterns; and (b) in a heating and cooling mode in the temperature range of 400 – 1100 °C and 2 Theta range from 26.4° to 35.4°.

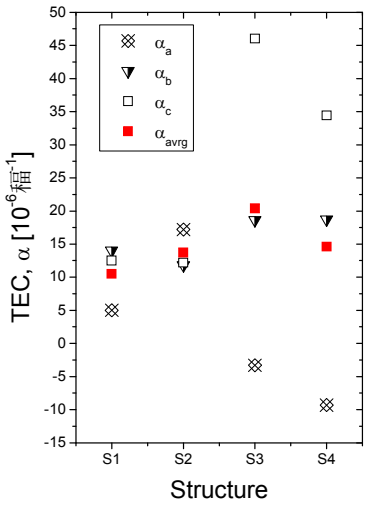

Figure 4. Microscopic thermal expansion coefficients in the three spatial directions (α_a, α_b, α_c) and the average value α_{avrg} for $La_6W_2O_{15}$ determined from the HT–XRD study.

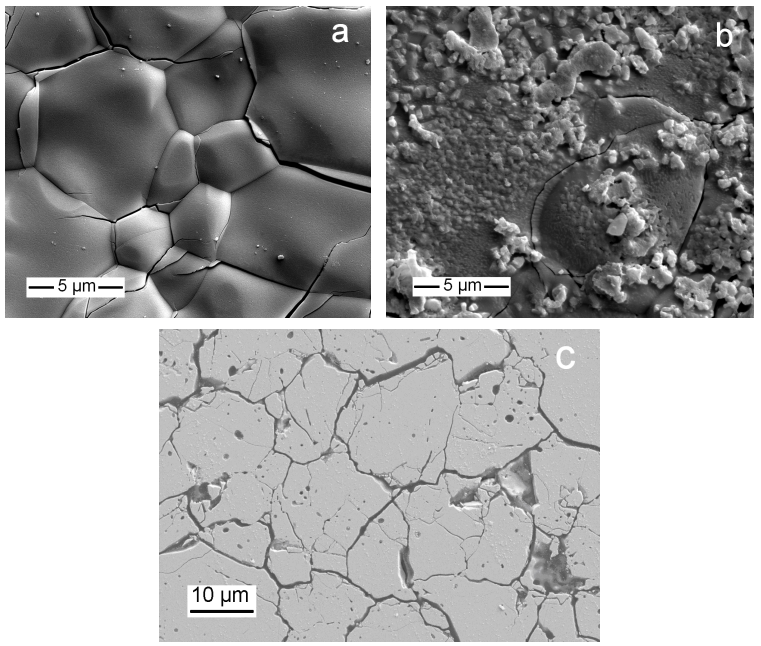

Figure 5. Microstructure of $La_6W_2O_{15}$. SEM images of (a) as sintered specimen; (b) unpolished surface after conductivity measurements and (c) polished surface after conductivity measurements.

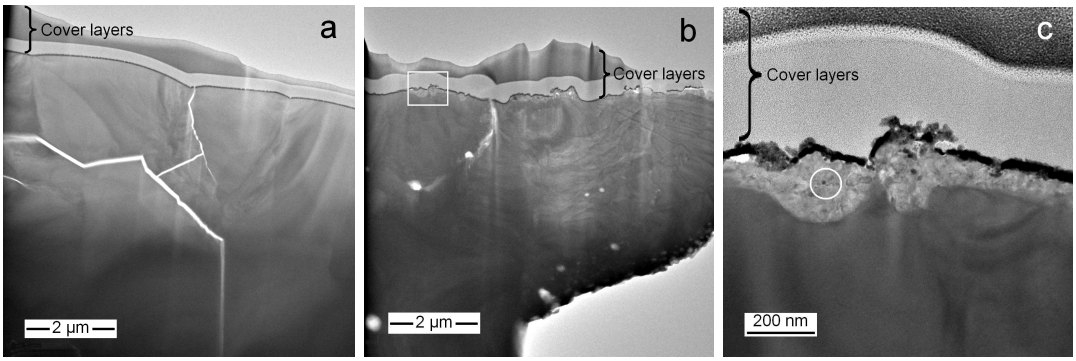

Figure 6. TEM bright–field micrographs of $La_6W_2O_{15}$ show specimen cross–sections. The sample was investigated before (a) and after conductivity measurements (b). Area indicated with a white rectangle in (b) is shown at higher magnification in (c). The white circle marks the region at which the EDX measurements were performed.

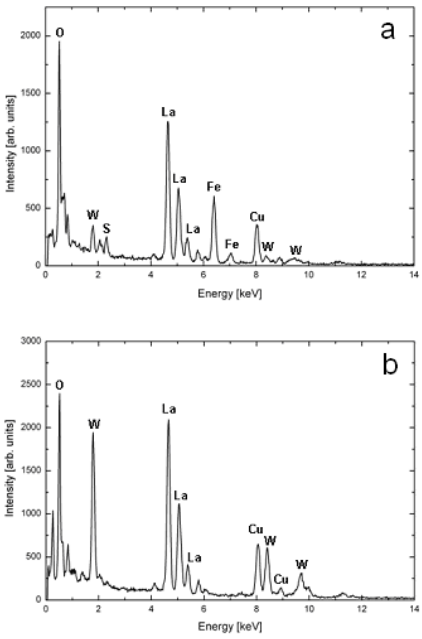

Figure 7. EDX spectra taken at the surface precipitate (a) (cf. Fig. 6 (c)) and the bulk (b) of the $La_6W_2O_{15}$ sample after conductivity measurements.

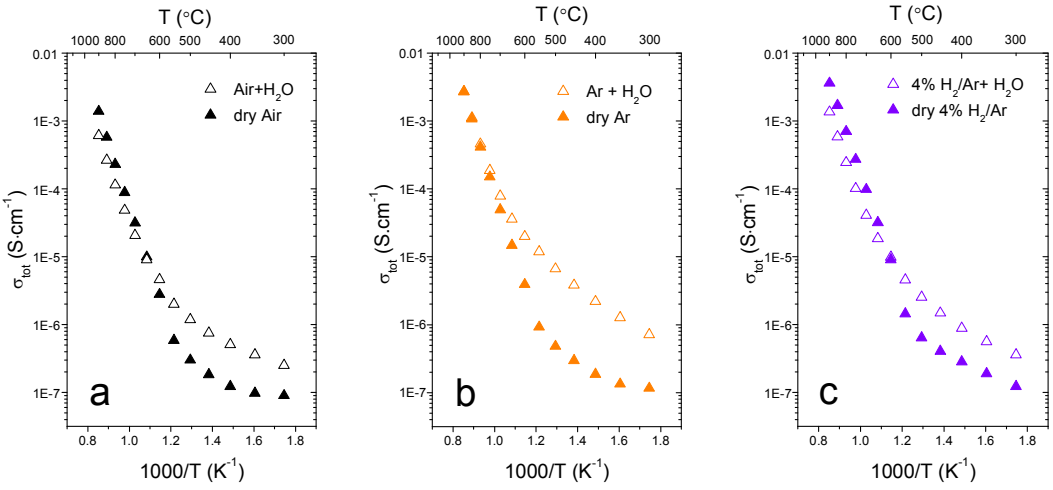

Figure 8. Total electrical conductivity of $La_6W_2O_{15}$ measured as a function of the inverse temperature at fixed frequency (11.9 kHz) under wet and dry a) synthetic air; b) Ar; c) mixture of 4% H_2 in Ar.

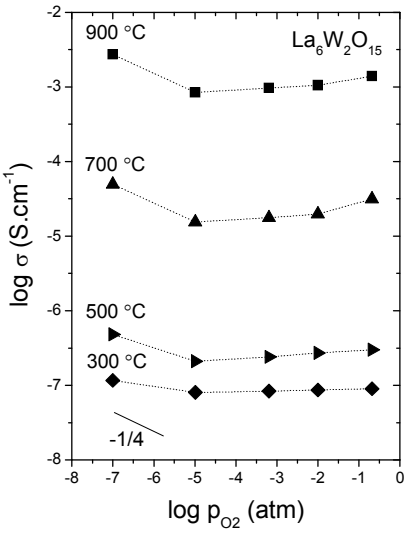

Figure 9. Total electrical conductivity of the $La_6W_2O_{15}$ at 11.9 kHz as a function of p_{O2} in dry atmosphere.

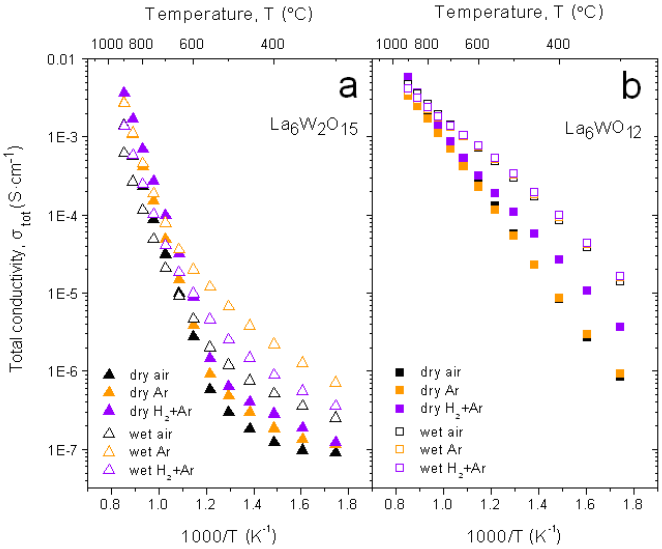

Figure 10. Total electrical conductivities of $La_6W_2O_{15}$ (a) and LWO (b) as a function of the inverse temperature at 11.9 kHz under wet and dry conditions in different atmospheres (synthetic air, Ar and mixtures of 4% H_2 in Ar).

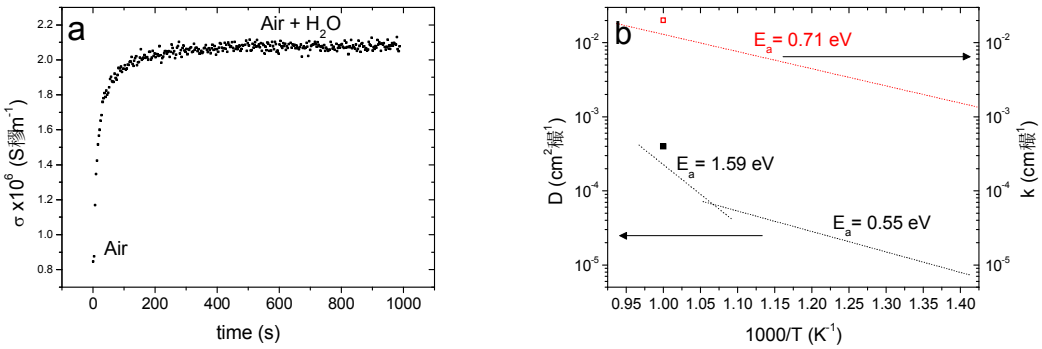

Figure 11. (a) *dc*–conductivity of $La_6W_2O_{15}$ at 450 °C as a function of time when the atmosphere is switched from dry air (p_{O2} = 0.21 atm) to wet air (p_{H2O} = 0.025 atm, p_{O2} = 0.21 atm); (b) surface exchange coefficient (k) and diffusion coefficient (D) for hydration process plotted as a function of the temperature.

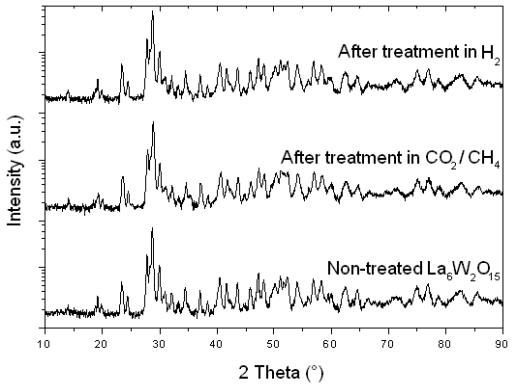

Figure 12. Diffraction patterns of $La_6W_2O_{15}$ before and after exposure to the carbonation test at 750 °C for 72 h and the reduction test at 900 °C for 55 h.

Chemistry and Materials Research
ISSN 2224- 3224 (Print) ISSN 2225- 0956 (Online)
Vol 2, No.1, 2012

ASSOCIATED CONTENT

Supporting Information

Figure S1

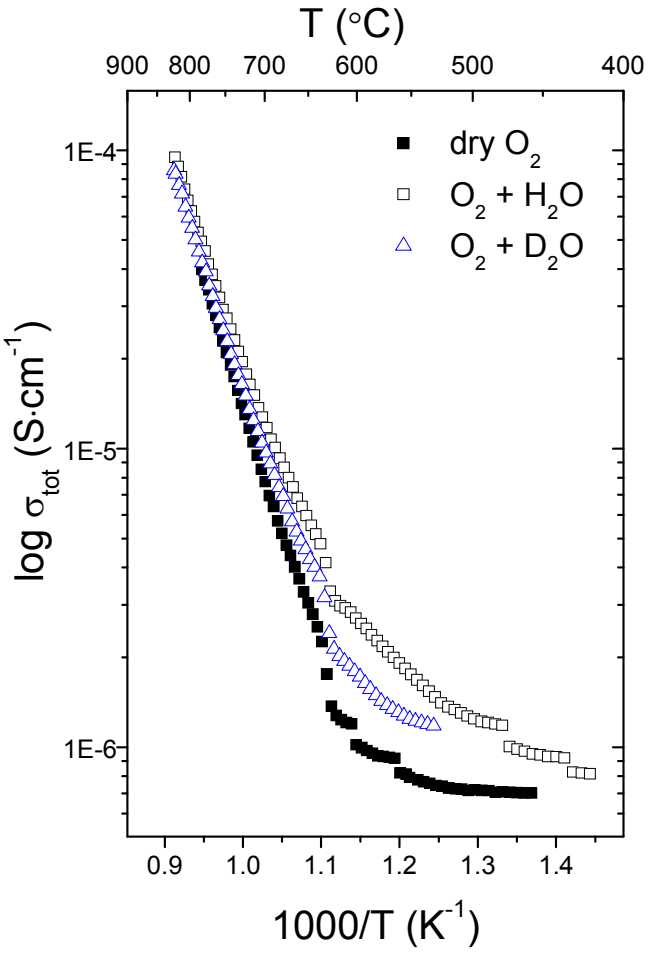

Figure S1. Total electrical conductivity of $La_6W_2O_{15}$ measured as a function of the inverse temperature at fixed frequency of 100 Hz in dry O_2 and in O_2 moisturized with 2.5 vol. % H_2O and 2.5 vol. % D_2O.

Figure S2

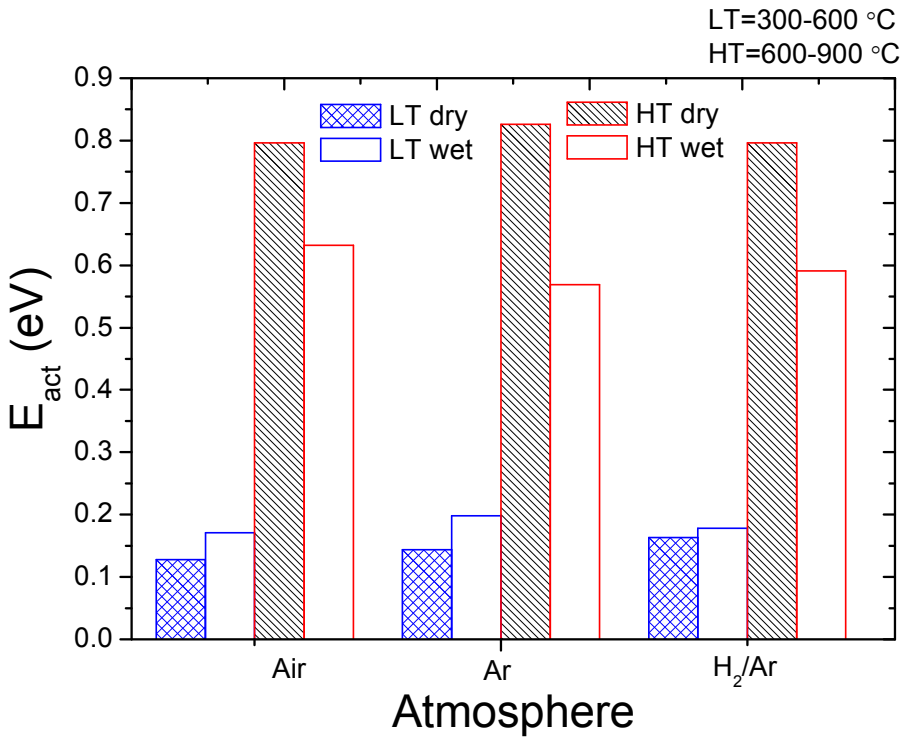

Figure S2. Activation energies for the total conductivity of $La_6W_2O_{15}$ in different wet and dry atmospheres.

Figure S3

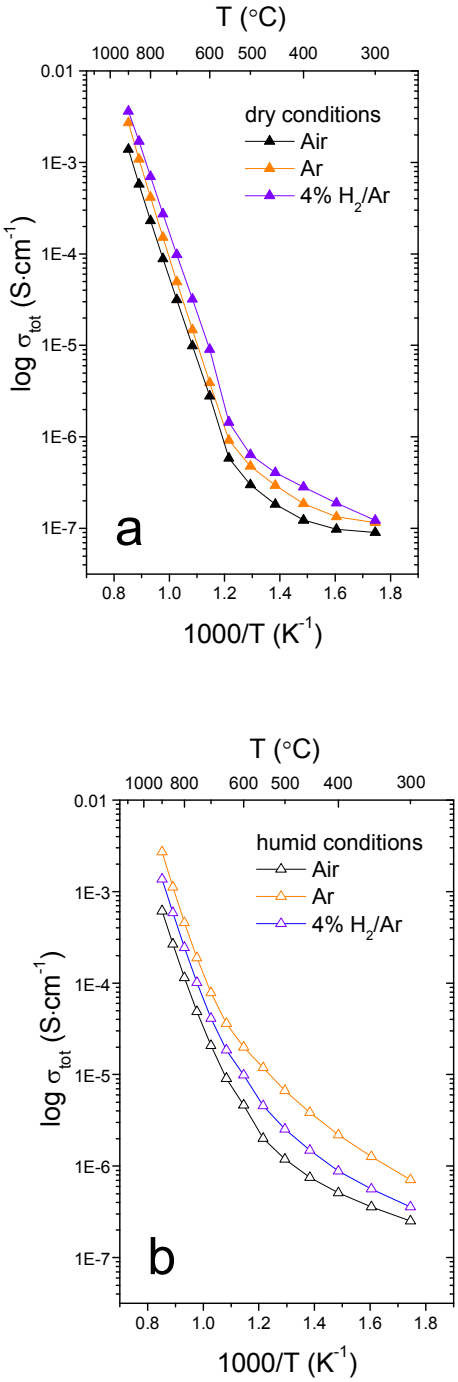

Figure S3. Total electrical conductivity of $La_6W_2O_{15}$ measured as a function of the inverse temperature at fixed frequency of 11.9 kHz in dry (a) and wet (b) conditions.

Figure S4

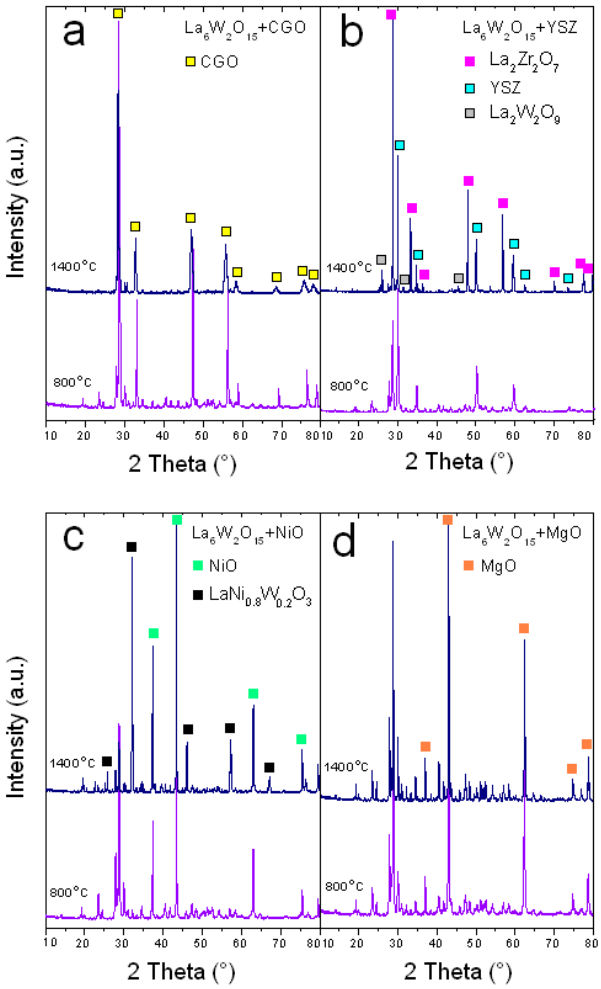

Figure S4. Diffraction patterns of the reaction product(s) of $La_6W_2O_{15}$ with a) CGO; b) YSZ; c) NiO; d) MgO at 800 °C/12h and 1400 °C/12h.